symmetry

MDPI

Article

Design and Biomechanical Properties of Symmetrical Lumbar Fusion Cage Based on Lightweight Titanium Alloy Flexible Microporous Metal Rubber

Juan Xiao [1,2], Tianqi Zhu [1,3], Linlin Li [3], Liangliang Shen [1,4], Zhiying Ren [3,*] and Jian Xu [1,4,*]

[1] Ningbo Institute of Materials Technology and Engineering, Chinese Academy of Sciences, Ningbo 315201, China; xiaojuan21@mails.ucas.ac.cn (J.X.); 210227100@fzu.edu.cn (T.Z.); llshenlyndon@mail.dlut.edu.cn (L.S.)
[2] University of Chinese Academy of Sciences, Beijing 100049, China
[3] School of Mechanical Engineering and Automation, Fuzhou University, Fuzhou 350116, China; 220210009@fzu.edu.cn
[4] State Key Laboratory of Fine Chemicals, Liaoning High Performance Polymer Engineering Research Center, School of Chemical Engineering, Dalian University of Technology, Dalian 116024, China
* Correspondence: t06027@fzu.edu.cn (Z.R.); xujian1028@dlut.edu.cn (J.X.)

Abstract: In recent years, the incidence rate of lumbar diseases has been progressively increasing. The conventional lumbar fusion cages used in existing lumbar interbody fusion surgery are not able to take into account the multiple characteristics of cushioning, vibration reduction, support, cell adhesion, and bone tissue growth. Therefore, in this work, based on the CT data of a lumbar intervertebral disc plain scan, a combined symmetric lumbar fusion cage structure was innovatively designed. The core was made of lightweight TC4 medical titanium alloy flexible microporous metal rubber (LTA-FMP MR), and the outer frame was made of cobalt–chromium–molybdenum alloy. Its comprehensive biomechanical performance was comprehensively evaluated through finite element simulation, static and dynamic mechanics, and impact resistance tests. The three-dimensional model of the L3/L4 lumbar segment was established by reverse engineering, and a Mises stress analysis was conducted on the lumbar fusion cage by importing it into Ansys to understand its structural advantages compared to the traditional lumbar fusion cage. Through static experiments, the influence of the internal nucleus of a symmetrical lumbar fusion cage with different material parameters on its static performance was explored. At the same time, to further explore the superior characteristics of this symmetrical structure in complex human environments, a biomechanical test platform was established to analyze its biomechanical performance under sinusoidal excitation of different amplitudes and frequencies, as well as impact loads of different amplitudes and pulse widths. The results show that under different amplitudes and frequencies, the lumbar fusion cage with a symmetrical structure has a small loss factor, a high impact isolation coefficient, and a maximum energy consumption of 422.8 N·mm, with a maximum kinetic energy attenuation rate of 0.43. Compared to existing traditional lumbar fusion cages in clinical practice, it not only has sufficient stiffness, but also has good vibration damping, support, and impact resistance performance, and has a lower probability of postoperative settlement, which has broad application prospects.

Keywords: symmetrical lumbar fusion cage; metal rubber; biomechanics; dynamic performance; impact resistance

Citation: Xiao, J.; Zhu, T.; Li, L.; Shen, L.; Ren, Z.; Xu, J. Design and Biomechanical Properties of Symmetrical Lumbar Fusion Cage Based on Lightweight Titanium Alloy Flexible Microporous Metal Rubber. *Symmetry* **2023**, *15*, 1938. https://doi.org/10.3390/sym15101938

Academic Editors: Guangdong Tian, Yong Peng, Zhiwu Li, Amir M. Fathollahi-Fard and Honghao Zhang

Received: 21 September 2023
Revised: 14 October 2023
Accepted: 17 October 2023
Published: 19 October 2023

1. Introduction

Lumbar degenerative diseases are one of the main causes of patients with low back pain or functional impairment of lower limbs. Currently, lumbar interbody fusion (LIF) surgery is one of the most effective treatments for this condition in clinical practice, aiming to restore the physiological curvature of the lumbar spine, stabilize the vertebrae, and limit

the abnormal movement between vertebral bodies and relieve the pain and numbness in the lower back and legs [1,2]. The main indications for lateral LIF include lumbar segmental instability, mild spinal stenosis, discogenic low back pain, and posterolateral postoperative recurrence combined with scoliosis [3,4]. For patients with minor injuries or lesions in the L1–L4 lumbar segments, lateral LIF provides thorough decompression and corrective effects. Due to its minimally invasive nature, lateral LIF results in smaller surgical trauma and significantly lower incidence of complications such as nerve root injury and persistent pain, compared to posterior and anterior LIF surgeries [5].

As an important part of the LIF process, the fusion device is mainly used to restore the height and physiological curvature of the lumbar intervertebral space, achieve immediate postoperative stability, reduce the occurrence of pedicle screw breakage, promote intervertebral bony fusion, and reduce the amount of removed autologous bone to a certain extent. As a result, the occurrence of a series of complications caused by it can be minimized [6,7]. As an intervertebral implant, the symmetrical structural fusion device should not only be of similar size to the intervertebral disc, but also be made of materials with no cytotoxicity and good biocompatibility. Moreover, it should have an elastic modulus and strength similar to those of bone tissue, good wear and fatigue resistance, and be conducive to the growth of new bone tissue and achieve biomechanical stability [8] (Figure 1). Intervertebral implant materials commonly used in clinical practice can be roughly divided into autograft, allograft, nano-hydroxyapatite (n-HA), tantalum metal, polymeric, and bone-induced composite materials, among others. Nevertheless, the amount of autologous bone is limited, allogeneic bone and n-HA have a low fusion rate, tantalum metal has a high elastic modulus and strong stress shielding effect, polymers have poor antibacterial properties, which can easily lead to osteolysis and local inflammation, and bone-induced composite materials are prone to misplacement caused by postoperative fusion cage settlement. The limitations of these materials have hindered, to a certain extent, the further promotion and application of lumbar intervertebral fusion devices [9].

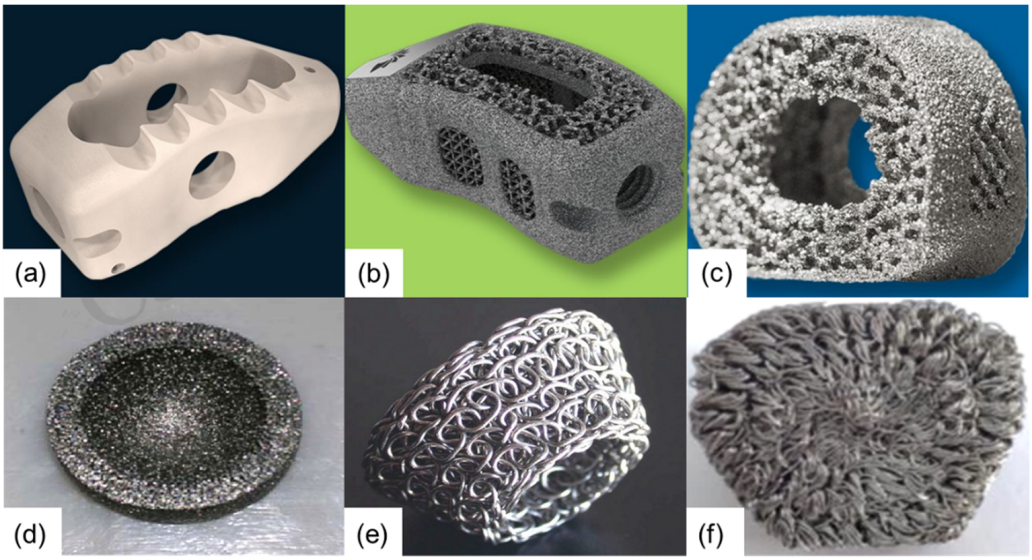

Figure 1. (**a**) PEEK-OPTIMA polymer spinal stabilization system; (**b**) threaded fusion; (**c**) anterior cervical intervertebral fusion; (**d**) metal rubber acetabular; (**e**) metal rubber ring; (**f**) metal rubber cervical disc.

Among several implant materials, titanium alloy has been widely used in the medical field due to its light weight, high strength, corrosion resistance, good biocompatibility, high osseointegration ability [10], and other advantages [11,12]. However, in clinical application, its high elastic modulus makes the fusion cage prone to subsidence after surgery; thus, the problem of stress shielding has gradually attracted certain attention [13].

In addition, porous titanium and its alloys, with the advantages of lower Young's modulus, ease of bone cell ingrowth, and mechanical properties similar to those of human bone, i.e., compressive strength, elastic modulus, and reduced stress shielding, are gradually being applied in the field of medical devices [14–16]. In clinical practice, in order to restore segmental alignment and balance, single or multiple fusion devices can be implanted depending on the intervertebral dimensions of the patient. For example, Liu et al. found no significant difference in the fusion rates between two fusion devices and a single fusion device through statistical analysis [17]. Herrera et al. used electron beam melting to prepare non-random lattice structures and performed characterization of the porous structures [18]. Harrysson et al. prepared titanium implants via electron beam melting, which had mechanical properties similar to those of human bone in terms of compressive strength, elastic modulus, as well as reduced stress shielding [15,16], good biocompatibility, and high osseointegration [13]. The popularity of 3D printing technology due to its high molding capacity, short processing cycle, customizability, and low cost [19] has driven the widespread use of titanium and its alloys in the medical field [20,21]. Tantalum has good biocompatibility [22,23] and high fusion rate, while porous tantalum has an elastic modulus similar to that of human bone, high bending strength [24], and good wear resistance [25]. However, when applied in posterior LIF surgery, the subsidence rate is relatively high [26].

Metal rubber (MR) is an elastic porous damping material produced through the winding and pressing of metal wires. As a symmetrical structural material, it has not only good elasticity, damping, and buffering properties, but also excellent properties such as high- and low-temperature resistance and corrosion resistance [27]. Moreover, the interpenetrating porous structure of the material facilitates cell adhesion and bone tissue growth, nutrient transport, and metabolism, and further reduces the overall mass while maintaining the required biomechanical stiffness, reducing its own stress masking effect, and providing new ideas for the design of fusion devices. In recent years, MR has been gradually applied to the medical field due to its excellent mechanical properties and flexible porous structure, which are conducive to bone cell growth. Fu Jiangbo and other scholars of the Harbin Institute of Technology applied MR to an artificial hip joint and performed friction tests with a steel ball on an artificial hip joint testing machine to simulate the actual frictional contact situation of its implantation in the body [28]. The team led by Zhai Wenjie considered the biomechanical requirement of artificial joint cartilage, which includes both good permeability and cushioning properties. They prepared a composite made of MR and polyvinyl alcohol hydrogel for the acetabulum and investigated its frictional performance. The results revealed that the friction torque was lower than that of the polytetrafluoroethylene acetabulum [29]. The team of Zhao Xianghao at the Harbin Institute of Technology applied MR to the cervical intervertebral disc, simulated the mobility of the model in ABAQUS, and verified its feasibility by implanting it into the cervical vertebrae of goats [30]. Overall, combining the excellent biocompatibility of titanium alloy with the unique structure and mechanical properties of MR, the lightweight titanium alloy flexible microporous MR (LTA-FMP MR) intervertebral fusion cage has broad application prospects.

In this paper, based on the excellent support, cushioning, vibration damping performance, wear resistance, and microporous structure characteristics of LTA-FMP MR, a symmetric combined LTA-FMP MR lumbar fusion cage is designed. Through finite element (FE) simulation, static-dynamic mechanics, and impact resistance tests, the present study investigates the effect of different material parameters of the MR core on the performance of a combined MR lumbar fusion device (LFD) under various working conditions. Its comprehensive biomechanical properties are evaluated, providing new insights into the further research and development of LFDs. The specific content is as follows: The Section 1 provides an overview of the current research status and limitations in the field of lumbar fusion cages. In Section 2, a three-dimensional structural model of the human lumbar spine segment is reconstructed using reverse engineering technology, and finite element simulation was employed to assess the stress within the lumbar spine fusion cage assembly under

various loading conditions. Section 3 focuses on investigating variances in the mechanical properties of metal rubber cores prepared with different parameters, with quasi-static tests conducted across various force gradient ranges. Section 4 involves a comprehensive analysis of the biomechanical performance of the fusion device under different amplitudes, pulse widths, and frequencies. Finally, in Section 5, the study's findings and conclusions are summarized and discussed.

2. LFD Design and Stress Analysis

By improving the lumbar computed tomography (CT) measurement method, effective measurement of the vertebral body spacing between the L3/L4 segments of the human lumbar spine can be conducted, guiding the design of the LTA-FMP MR lumbar fusion cage combination structure. A three-dimensional structural model of the L3/L4 lumbar spine segments was developed via reverse engineering, and the stress distribution and von Mises stresses of the upper and lower bone endplates of the lumbar spine fusion cage assembly under various working conditions, e.g., forward bending, backward extension, bending, and torsion, were investigated, providing a reference for the subsequent biomechanical performance research on lumbar fusion cages.

2.1. LFD Structural Design

The symmetric fusion cage is a buffering and damping support device between adjacent vertebral cones of the lumbar spine; thus, its structural design needs to refer to the spacing between adjacent vertebral segments. As depicted in Figure 2a1, traditional lumbar CT measurement methods usually take the average value of the middle line and the front and rear lines of the vertebral body in the midsagittal position [31]. However, due to the concave nature of the vertebral end face, the quality of the measured data is generally low, resulting in a designed fusion cage with a smaller size than the actual one, which increases the risk of postoperative fusion cage displacement. To evaluate the distance between adjacent vertebral bodies more accurately, Shilei et al. proposed an improved lumbar CT measurement method based on the traditional one (Figure 2a2), which provides a more realistic and accurate assessment of the adjacent vertebral spacing than conventional measurements. This is achieved by focusing on the central region of the lumbar spine, using the central line connecting the vertebral bodies in the median sagittal position as the baseline, measuring the vertebral spacing 5 mm anterior and posterior to it, and taking the average of these three values as the intervertebral height value [32].

In this work, a 24-year-old healthy male volunteer was selected to have a lumbar disc CT scan at Fujian Provincial Hospital, and the lumbar cone spacing at the L3/L4 segment was measured by the modified lumbar CT measurement method. Figure 2a3,a4 exhibit the measurements of the distance between the L3/L4 vertebral bodies and the cross-section of the L4 cone, respectively. The intervertebral spacing at the center of the vertebral body in the midsagittal position and at a distance of 5 mm before and after it was 13.43 mm, 14.94 mm, and 13.68 mm, respectively, with an average value of 14.02 mm; the transverse length of the vertebral body was 53.31 mm, and the longitudinal dimension was 38.42 mm.

The design of a symmetric lateral lumbar fusion cage should meet not only the size requirements, but also the usage requirements after implantation into the human lumbar spine. To better analyze its mechanical properties under various operating conditions, the obtained CT data were imported into the Mimics software in DICOM format, and reverse engineering was performed to convert the 2D CT images of L3/L4 lumbar spine segments into a 3D structural model (Figure 2a5). Furthermore, in order to facilitate further analysis, surface hole filling and smooth repair were performed on the 3D model, resulting in a repaired 3D model (Figure 2a6).

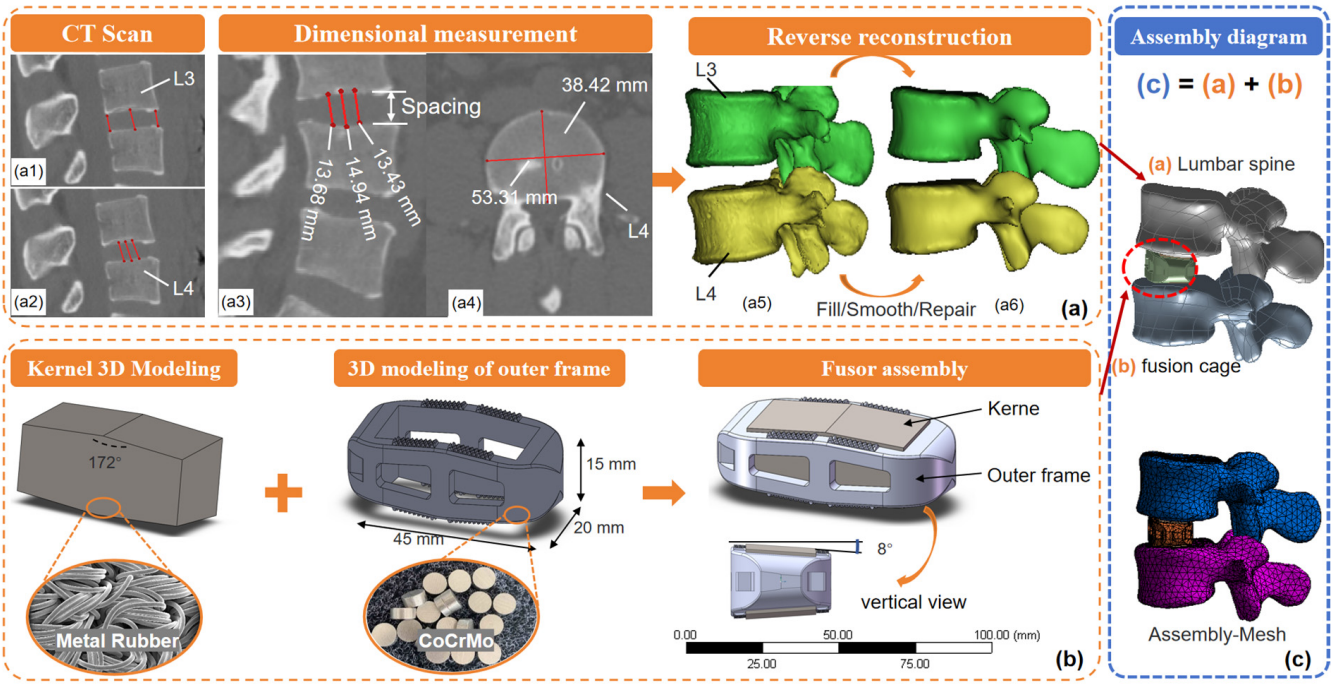

Figure 2. 3D modeling process of lumbar vertebrae and fusion apparatus: (**a**) Construction of three-dimensional model of lumbar spine: (**a1**) Traditional CT measurement method; (**a2**) improved CT measurement method; (**a3**) L3/L4 lumbar spinal cone spacing measurement map; (**a4**) L4 cone cross-section measurement diagram; (**a5**,**a6**) L3/L4 lumbar segment three-dimensional model; (**b**) 3D model of the lumbar fusion cage; (**c**) assembly drawing of the L3/L4 lumbar spine segment fusion cage.

The structural design of the symmetric lumbar fusion cage was performed based on the lumbar intervertebral space parameters obtained by the improved lumbar CT measurement method. Considering the convenience of the production and processing of the fusion cage, a combined structure was adopted. The core of the LTA-FMP MR fusion cage was made of TC4 medical titanium alloy wire, which not only has good elasticity and damping performance, but also its internal micropore structure (Figure 2b) is conducive to bone cell adhesion and bone tissue growth, increasing the probability of successful surgery. The core was shaped like a cuboid with an angle of 8° between the front and rear ends of its upper and lower surfaces. The outer frame of the fusion cage was made of CoCrMo with toothed protrusions distributed on both sides of its upper and lower surfaces, in order to increase the friction between the fusion cage and the lumbar vertebral body, reduce the probability of postoperative slip, and increase the fusion cage stability. For the convenience of implantation during surgery, the front end of the fusion cage was designed with a bullet head, taking into account the physiological protrusion of the lumbar spine. The angle between the front and rear surfaces of the fusion cage was 8°, providing it with a structural feature of high front and low back. To facilitate the clamping of the lumbar fusion cage during surgery, two clamping slots were opened on one side. Moreover, there were large bone grafting windows on both sides of the outer frame of the fusion cage to facilitate bone cell growth after its implantation. The LTA-FMP MR core and the CoCrMo frame were connected by pressing, and the stable connection between them was ensured by interference fit. Figure 2b presents the three-dimensional model of a lateral lumbar fusion cage. The outer frame of the lumbar fusion cage was 45 mm long and 20 mm wide, and its front end was 15 mm high. The angle between the front and rear ends of the upper and lower surfaces was 8°, and that between the left and right sides was 172°. The upper and lower surfaces of the outer frame were designed with 0.5 mm high toothed protrusions on both sides, and there were four trapezoidal bone grafting windows on the front and rear

surfaces (4 mm on the upper bottom; 6 mm on the lower bottom; 12 mm in height). The right terminal bullet of the fusion device was designed as a semicircular arc with a diameter of 20 mm. The transition between the upper and lower surfaces was realized through a circular arc. A clamping groove with a length of 5 mm, width of 4 mm, and height of 4 mm was opened on the left end side, and a through groove with a length of 31 mm and width of 14 mm was opened inside to facilitate the installation of the LTA-FMP MR core. To fully utilize the unique elasticity and damping performance of the LTA-FMP MR core, its upper and lower surfaces were 0.5 mm higher than the outer frame of the lumbar fusion cage, with a length of 31 mm, width of 14 mm, and height of 16 mm at the front end. The angle between the front and rear ends of the upper and lower surfaces was 8°, and that between the left and right sides was 172°.

Subsequently, the 3D model was imported into the FE analysis software ANSYS for mesh generation and assembly with the lumbar fusion cage to perform simulations under various working conditions, as shown in Figure 2c.

2.2. Stress Analysis of L3/L4 Segment Lumbar Spine and Fusion Cage

The outer frame of the lumbar spine fusion cage was composed of CoCrMo, and the inner core of the fusion cage was composed of LTA-FMP MR made of TC4 medical titanium alloy wire. To truly reflect the stress situation after the implantation of the lumbar spine fusion cage (Figure 3a), an axial compression force of 500 N was applied to the upper surface of the L3 vertebral body to simulate the axial compression force experienced by the human body in daily life. Considering that the human lumbar spine is often in several motion states, e.g., forward bending, backward extension, bending, and rotation, a torque of 10 N·m in different directions was applied to the upper surface of the L3 vertebral body (Figure 3b) and fixed constraints were set to the lower surface of the L4 vertebral body to limit its six degrees of freedom (Figure 3c), facilitating the simulation of its mechanical properties under various motion states [33,34]. The contact type between the metal rubber core and the outer frame of the fusion apparatus is set to Bonded Contact, the contact type between the lumbar bone and the fusion apparatus is set to Frictional Contact, and the friction coefficient is set to 0.3. The material performance parameters are shown in Table 1.

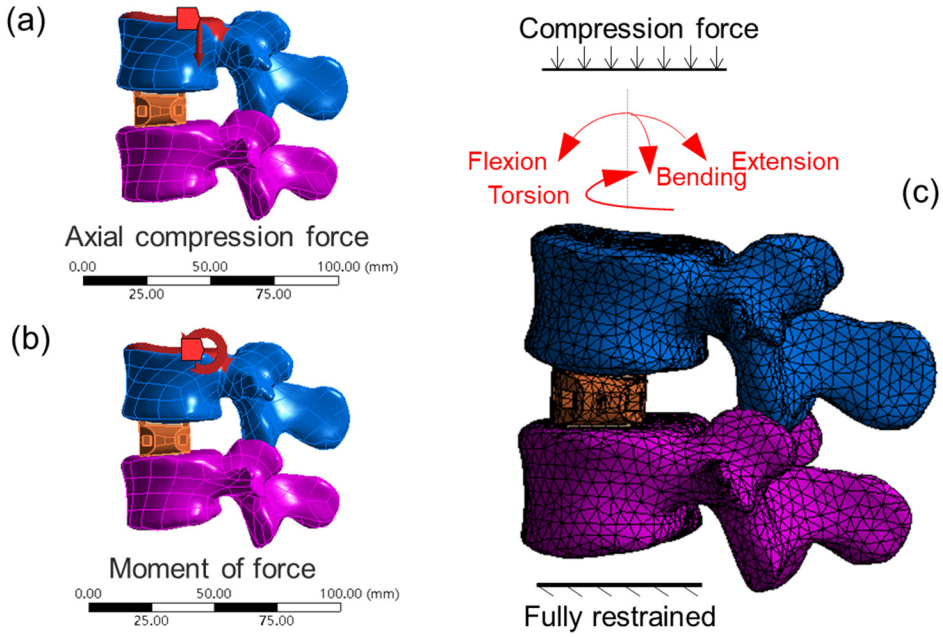

Figure 3. Loading situation and boundary conditions: (**a**) diagram of axial compression force; (**b**) torque diagram; (**c**) boundary condition setting. (Blue is lumbar L3, purple is lumbar L4, orange is lumbar fusion apparatus).

Table 1. Material properties parameter table.

Materials	Young's Modulus (Mpa)	Poisson's Ratio
CoCrMo	116,000	0.3
Metal Rubber	145	0.47
Bone	12,000	0.3

The stress distribution on the upper and lower vertebrae endplates can reflect the possible tendency of the lumbar fusion cage to sink after implantation, while the peak stress reflects the stress concentration on the bone endplate. The occurrence of stress concentration can increase the probability of fusion cage sinking [35]. Figure 4 illustrates the stress distribution of the upper and lower vertebrae endplates under various conditions, i.e., forward bending, backward extension, left bending, right bending, and torsion. In Figure 4a–d, it can be observed that, during forward flexion, the stress on the upper and lower bone endplates was mainly concentrated at the front, with maximum stresses of 4.21 MPa and 4.62 MPa, respectively. Under posterior extension, the stresses on the upper and lower bone endplates were mainly concentrated at the posterior part, with maximum stresses of 7.28 MPa and 7.79 MPa, respectively. The peak stresses on the upper and lower bone endplates increased by 73% and 69%, respectively, under backward extension compared to those under forward bending. In Figure 4e–h, it can be observed that, during left bending, the stress on the upper and lower bone endplates was mainly concentrated at the left posterior region, with maximum stresses of 5.24 MPa and 5.95 MPa, respectively. During posterior bending, the stress on the upper and lower bone endplates was mainly concentrated at the right posterior region, with maximum stresses of 5.50 MPa and 4.02 MPa, respectively. Compared to that under left bending, the peak stress on the upper bone endplate increased by 5.0% during right bending, while that on the lower bone endplate decreased by 32.4%. According to Figure 4i,j, during torsion, the stress on the upper bone endplate was mainly concentrated at the rear, with a maximum stress of 5.38 MPa, while the stress distribution on the lower bone endplate was relatively uniform, with the maximum stress located at the lower left corner of the lower bone endplate, reaching a value of 5.94 MPa.

Figure 5a presents the statistical comparison of peak stresses in the upper and lower bone endplates under different loading conditions. It can be observed that, under different loading conditions, the peak stresses on the upper and lower bone endplates were basically the same. Except for the right bending loading case, the peak stress on the lower bone endplate was 26.9% lower than that on the upper one, and the increase rate of the peak stress on the bone endplate was about 10% compared to that on the upper bone endplate under other loading conditions. In addition, it can be observed that the peak stress of the upper and lower bone endplates during extension was significantly higher than that under the other loading conditions. Wang et al. designed four types of fusion devices based on topology optimization and selected the group with the best peak comprehensive stress value of the upper and lower bone endplates; their results are compared with the data obtained in this paper. Since no difference between left and right bending was found, this paper recorded the mean value of the peak stress value of the upper and lower bone endplates of left and right bending as bending, and Figure 5b compares the obtained data. It was found that the peak stress of the upper and lower bone endplates of the lumbar fusion cage designed in this article was significantly lower than that reported in the relevant literature [36], indicating that the designed structure is reasonable and effective, and the probability of fusion cage sink is significantly reduced.

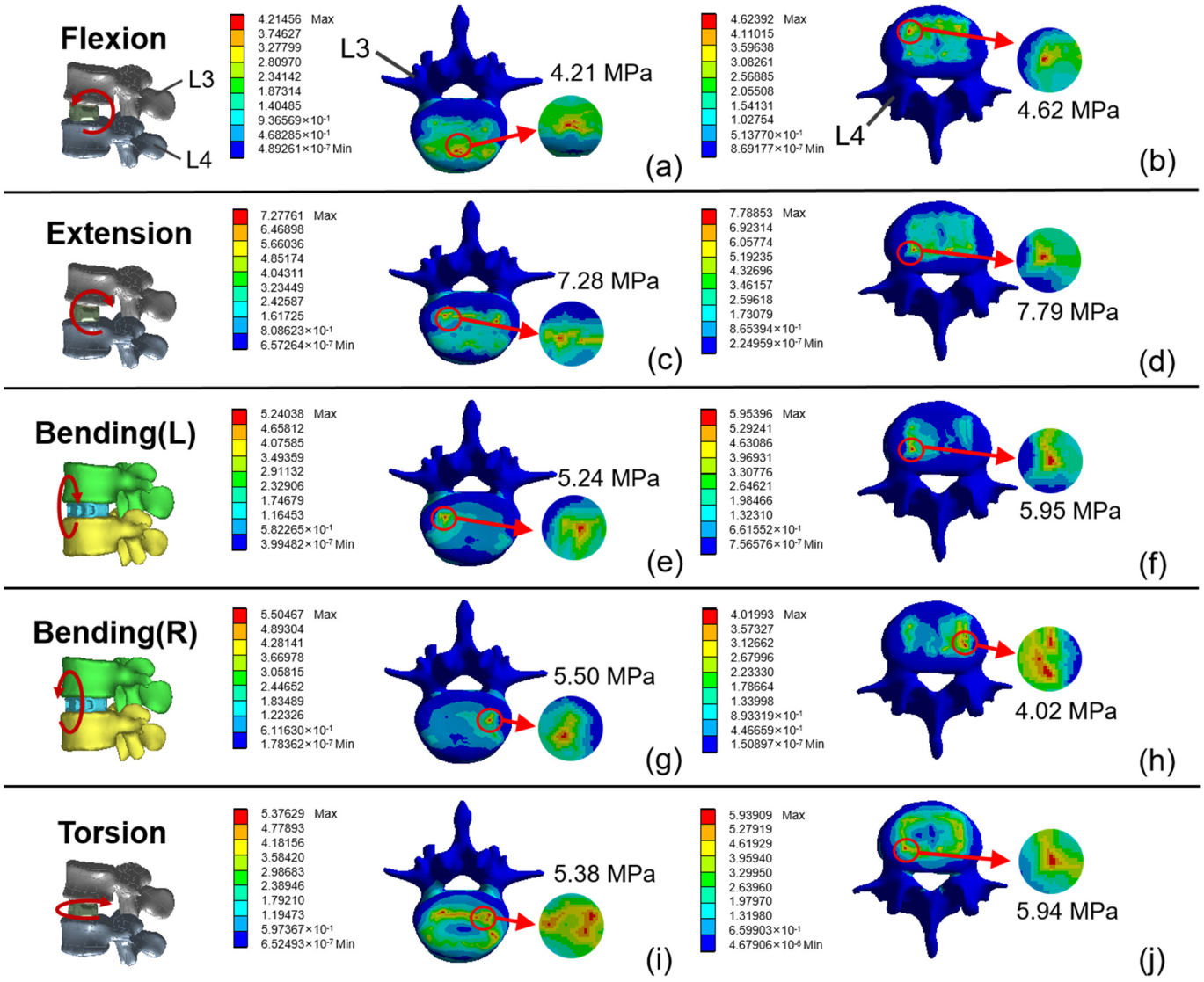

Figure 4. Stress distribution on the upper and lower vertebrae endplates under different loading conditions: (**a**,**b**) Stress distribution of upper and lower vertebral endplates during flexion; (**c**,**d**) Stress distribution of upper and lower vertebral endplates during extension; (**e**,**f**) Stress distribution of upper and lower vertebral endplates during bending(L); (**g**,**h**) Stress distribution of upper and lower vertebral endplates during bending(R); (**i**,**j**) Stress distribution of upper and lower vertebral endplates during torsion.

Intervertebral implants may also face the risk of collapse after surgery. Von Mises stress is a commonly used evaluation factor for the risk of intervertebral implant collapse. In general, the lower the peak von Mises stress, the lower the risk of collapse after lumbar fusion cage implantation. Analyzing the von Mises stress of the symmetric lumbar fusion cage under axial compression, forward bending, backward extension, left bending, right bending, and torsion (Figure 5d–j), it can be found that stress concentration existed mainly at the corners of the MR core of the fusion cage and the front edge of the outer frame. Figure 5c depicts the von Mises peak stress histogram of the fusion device under various loading conditions. It can be observed that the peak von Mises stress was significantly higher during forward bending and backward extension than during the other loading conditions, with values of 30.34 MPa and 41.53 MPa, respectively. However, the overall peak stress under various loading conditions was significantly lower than the 203 MPa

reported in the relevant literature [36], indicating that the risk of collapse may be lower after implanting the lumbar fusion cage designed in this paper.

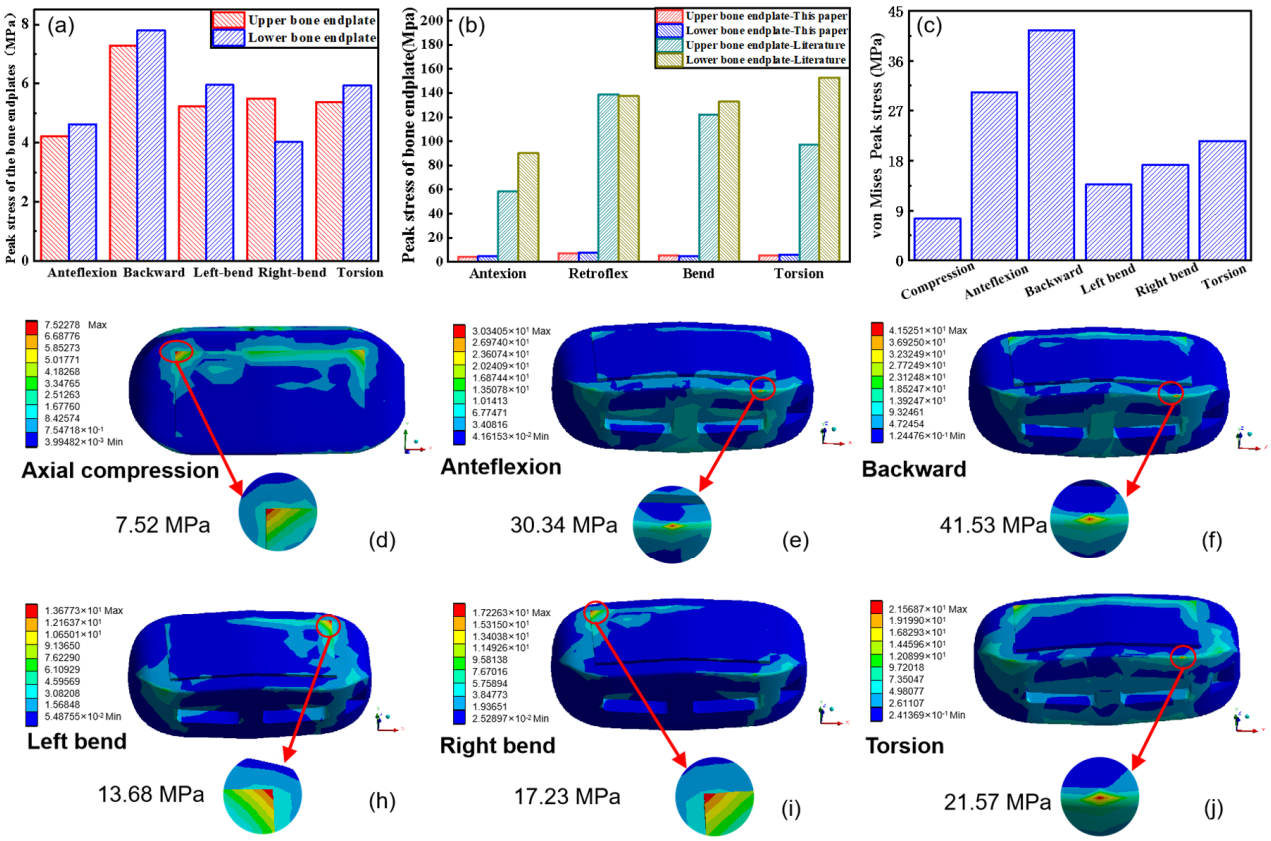

Figure 5. Simulated cloud image of lumbar fusion apparatus: (**a**) Peak stress of bone endplate under different loads; (**b**) comparison of peak stress of bone endplate under different loads with relevant literature [36]; (**c**) von Mises stress peak of the fuse under different loading conditions; (**d**–**j**) von Mises stress distribution diagram of the fusion device under different loading conditions.

3. Preparation and Quasi-Static Test of Lumbar Fusion Cage Core

To investigate the differences in mechanical properties of metal rubber cores with different preparation parameters, metal rubber cores with different relative densities and materials were prepared. Quasi-static tests were conducted under different force gradient ranges to investigate their energy dissipation mechanism under load and the changes in contact state between internal wire turns. The changes in energy dissipation, loss factor, and static stiffness of metal rubber cores with load were analyzed.

3.1. Preparation Process of Lumbar Fusion Cage Core

The core of the lumbar fusion cage was made of LTA-FMP MR. The preparation process is as follows. First, the wire of suitable material and diameter was selected according to the use environment and load-bearing requirements. Then, the wire was wound into a certain diameter metal spiral coil by special winding equipment (Figure 6a Pretreatment stage), after which it was stretched with a fixed pitch and the blank was wound on an MR blank automatic winding equipment (Figure 6b Blank forming stage). Subsequently, the wound blanks were cold stamped into a mold to obtain the required MR core sample (Figure 6c Stamping stage), which was finally ultrasonically cleaned and dried (Figure 6).

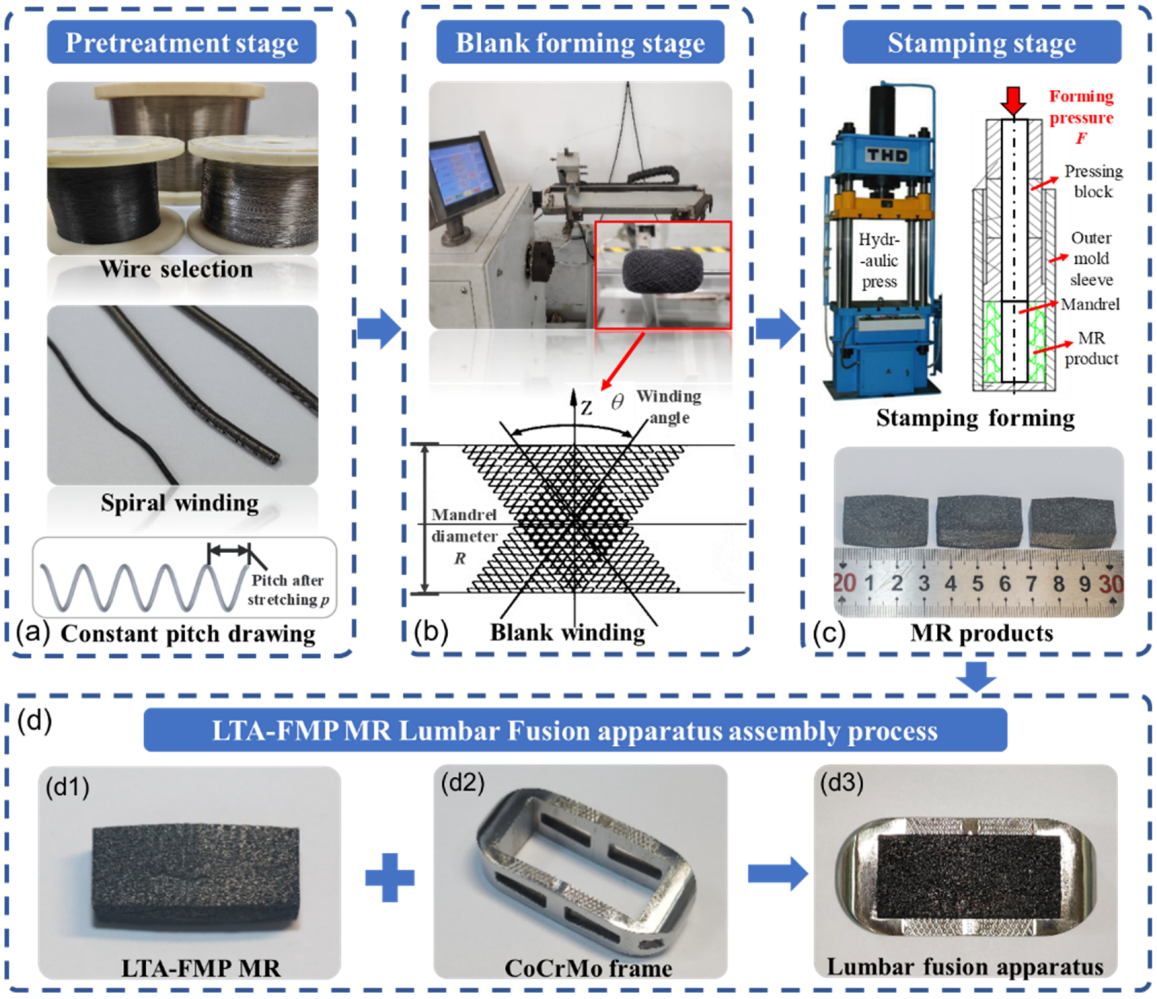

Figure 6. Flow chart of preparation of lumbar fusion cage core: (**a**) Pretreatment stage; (**b**) Blank forming stage; (**c**) Stamping stage; (**d**) LTA-FMP MR Lumbar Fusion apparatus assembly process.

In particular, good biocompatibility is the first concern, considering that the lumbar fusion cage should be implanted into the human body. In combination with the prevailing materials used in intervertebral implants, TC4 medical titanium alloy (Ti-6Al-4V) was selected to prepare the LTA-FMP MR core, while medical stainless steel (304) was employed to facilitate the subsequent comparative analysis of the mechanical properties of the two materials. In general, the higher the relative density of MR, the higher its stiffness, and the lower its relative density, the lower its load-bearing capacity. This characteristic should have different effects on the damping and vibration damping capacity of the material. To investigate the differences in the mechanical properties of MR cores with different relative densities, three MR cores with relative densities of 1.5 g/cm^3, 2.0 g/cm^3, and 2.5 g/cm^3 were prepared; the specific parameters of the samples are given in Table 2.

Table 2. Parameter table of lumbar fusion cage core sample.

Material	Wire Diameter (mm)	Relative Density (g/cm^3)	Mass (g)	Porosity	Sample Height (mm)
TC4	0.20	1.5	10.16	0.65	14.11
		2.0	13.54	0.53	13.95
		2.5	16.93	0.42	14.06
304	0.20	1.5	10.16	0.80	14.09
		2.0	13.54	0.74	14.08
		2.5	16.93	0.67	14.15

The prepared MR core is exhibited in Figure 6(d3). The outer frame of the lumbar fusion cage was combined with the core to obtain an MR lumbar fusion cage (Figure 6d).

3.2. Quasi-Static Experimental Study on the Inner Core of Lumbar Fusion Cage

To characterize the mechanical properties of the LTA-FMP MR core under load, quasi-static tests were conducted to investigate its energy dissipation mechanism under load and the changes in the contact state between internal wire turns. Quasi-static experiments with different force gradient ranges were conducted, and the energy dissipation, loss factor, and static stiffness changes of the LTA-FMP MR cores with load were analyzed. The test specimen was made of a medical TC4 titanium alloy MR core with a relative density of 2.0 g/cm^3, and the load was set to 100 N, 200 N, 300 N, 400 N, and 500 N to meet the majority of the fusion device usage requirements.

When the LTA-FMP MR core is subjected to an external load, the dry friction between its internal metal wires will lead to energy consumption. In a loading and unloading process, the energy ΔW dissipated by the MR can be calculated by the following equation:

$$\Delta W = \int_0^{x_{\max}} (F_{upload} - F_{unload}) dx \tag{1}$$

The energy U stored in the MR core during a loading and unloading process is:

$$U = \frac{1}{2} \int_0^{x_{\max}} (F_{upload} + F_{unload}) dx \tag{2}$$

where F_{upload} is the loading curve, F_{unload} is the unloading curve, $x_{\max}$ is the maximum deformation, and $F_{\max}$ is the load corresponding to the deformation $x_{\max}$.

In order to characterize the static mechanical properties of the LTA-FMP MR core, a static loss factor η and a static stiffness k are introduced, which can be calculated as follows:

$$\eta = \frac{\Delta W}{\pi U} \tag{3}$$

$$k = \frac{F_{\max}}{x_{\max}} \tag{4}$$

where ΔW is the dissipated energy, U stores internal energy, $F_{\max}$ is the maximum load, and $x_{\max}$ is the maximum displacement.

The quasi-static mechanical curves of the MR core obtained under different loads are presented in Figure 7a. It can be observed that the loading curve exhibited good consistency under different maximum loads, proving the performance stability of the MR core under different working conditions. Figure 7b presents the variation of the static parameters of the MR core under different loads. It was found that the energy dissipation and static stiffness of the MR core increased with increasing loading, which was due to the increased deformation of the MR as the load was increased. Moreover, the number of contact points between the inner wires increased (Figure 7e), the contact state changed from a sliding state to a relative sliding state, the friction between the wires increased, and the dissipated energy increased as well. At the same time, the deformation moved gradually from the soft phase to the exponential hardening phase, with more dry frictional contact between the internal wires than in the soft phase, resulting in increased stiffness. According to the variation diagram of the loss factor of the MR core under different loads, the loss factor gradually decreased with increasing load, while the change in its magnitude was not very significant, reflecting the long-lasting performance stability of the MR.

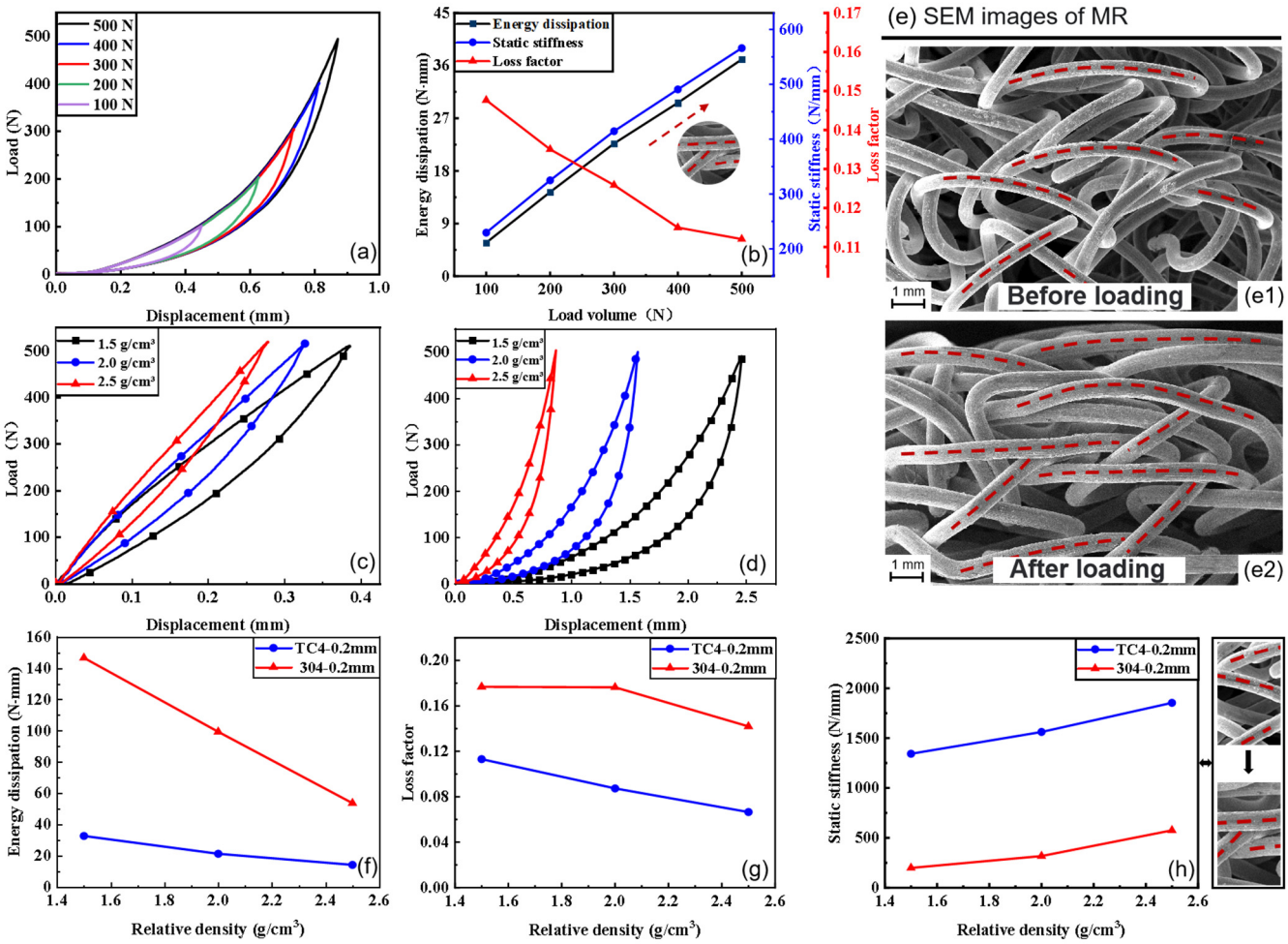

Figure 7. Metallic rubber inside approved static test results: (**a**) Variation of the static parameters of the TC4 MR under different loads; (**b**) quasi-static mechanical curves of TC4 MR under different loads; (**c**) quasi-static mechanical curve of TC4-0.2 mm MR core; (**d**) quasi-static mechanical curve of 304–0.2 mm MR core; (**e**) SEM micrograph of a MR core: (**e1**) before loading, (**e2**) after loading; (**f**–**h**) static parameters of MR cores with different relative densities.

As mentioned earlier, quasi-static tests were performed on six MR cores made of different materials with different relative densities. Figure 7c,d demonstrate the quasi-static mechanical curves of the MR prepared by 0.2 mm TC4 and 0.2 mm 304 with different relative densities, respectively. Good energy dissipation characteristics were observed, and the variation of the energy dissipation, loss factor, and static stiffness parameters with relative density for each sample was statistically obtained (Figure 7f–h). In Figure 7f, it can be seen that the MR core energy dissipation tended to decrease with increasing relative density for both TC4 and 304 materials. This is due to the fact that the lower the relative density of the MR core, the lower its stiffness, and the easier it is to enter the exponential hardening phase of deformation under the same load. The contact characteristics changed from soft to hard contact, leading to a significant increase in energy consumption. Figure 7g plots the variation of the loss factor of MR cores with different relative densities. It can be observed that, with the increase of the relative density, the loss factor of the MR core gradually decreased. On the other hand, for the same density and wire diameter, the loss factor of the TC4 MR core was much smaller than that of the 304 one, indicating that the durability performance of TC4 was almost excellent. Figure 7h shows the static stiffness variation of the MR core for different relative densities. It was found that the static stiffness of both the 304 and TC4 MR cores tended to increase with increasing relative density. This is due to the fact that the higher the relative density of the material, the more the contact

points between the turns of the filaments inside the MR, which are more constrained during deformation as indicated by the increased stiffness; for the same density and diameter, the static stiffness of 304 was significantly lower than that of TC4.

4. Biomechanical Properties of Lateral Lumbar Fusion

In order to assess the dynamic loads of lumbar fusion in daily life, the mechanical properties of lumbar fusion under different amplitudes and frequencies were analyzed. The loading dynamics of lumbar fusion were tested under sinusoidal excitation, and a loss factor was introduced to evaluate it. At the same time, considering the inevitability of impact loads on the lumbar spine during motion and sudden events, the impact resistance of lateral access LFDs with two material cores was tested under impact loads with different excitation amplitudes and pulse widths. The introduction of the impact isolation coefficient and kinetic energy decay rate can provide insight into the impact-resistant biomechanical performance of the lumbar fusion cage, leading to a more comprehensive assessment of the dynamic performance of lateral access LFDs.

4.1. Dynamics of Lateral Lumbar Fusion

The MR LFDs made of TC4 and 304 with three different relative densities (1.5 g/cm^3, 2.0 g/cm^3, and 2.5 g/cm^3) were subjected to sinusoidal excitation loading by means of a high- and low-temperature dynamic and static universal testing machine. The LFD was clamped in the upper and lower jigs of the machine in order to eliminate the residual stress inside it. Each specimen was preloaded for 5 min before the formal test and then tested; the data from the 30th test after the curve had been stabilized were taken as the test result.

The maximum elastic potential energy W in one loading cycle and the dissipated energy ΔW in one loading cycle can be calculated by:

$$W = \frac{1}{4}(F_{\max} - F_{\min})X_0 \tag{5}$$

$$\Delta W = -\omega X_0 \int_0^T F \sin(\omega t + \alpha) dt \tag{6}$$

where $F_{\max}$ and $F_{\min}$ are the maximum and minimum values of the discrete restoring forces collected during the test, respectively; X_0 and ω correspond to the amplitude and angular velocity of the excitation displacement; and α is the phase of the displacement at the beginning of the test.

The equivalent loss factor η can be obtained from the energy ΔW dissipated during one loading cycle and the maximum elastic potential energy W via the following equation:

$$\eta = \frac{1}{2\pi}\frac{\Delta W}{W} \tag{7}$$

4.2. Dynamic Test Results and Analysis

To analyze the effects of different materials, amplitudes, and vibration frequencies on the dynamic performance of the lumbar fusion cage, tests were designed using the control variable method to analyze the energy consumption, loss factors, and stiffness. The test parameters were set as shown in Table 3.

Table 3. Test parameter setting table.

Test Group	Material	Wire Diameter (mm)	Relative Density (g/cm^3)	Amplitude (mm)	Frequency (Hz)
Material	TC4/304	0.10	2.0	0.6	4
Amplitude	TC4	0.10	2.0	0.2/0.4/0.6/0.8/1.0	4
Vibration frequency group	TC4	0.10	2.0	0.6	1/2/3/4/5

The effects of amplitude, frequency, and material on the dynamic performance of the lumbar fusion apparatus are presented in Figure 8. In Figure 8a, it can be observed that the energy dissipation of the lumbar fusion cage increased gradually with increasing amplitude in the range of 0.2 to 1.0 mm. The loss factor decreased gradually with increasing amplitude, while the stiffness exhibited a trend of decreasing first and then increasing. That was due to the fact that when the amplitude increases, the deformation of the MR core increases, the contact points between the wires increase, and the contact state changes from sliding to relative sliding and parallel sliding, resulting in an increase in the energy dissipated by friction (Figure 8d–f) and the overall stiffness. Figure 8b illustrates the effect of frequency on the energy dissipation, stiffness, and loss factor of the lumbar fusion. As it can be observed, in the frequency interval from 1 Hz to 5 Hz, the stiffness of the LFD decreased gradually with increasing vibration frequency, while the loss factor gradually increased, and the energy dissipation exhibited a trend of increasing first and then decreasing. The effect of the material on the energy dissipation, stiffness, and loss factor of the lumbar fusion is presented in Figure 8c. It can be observed that, when all the other parameters were the same, the LFD prepared from TC4 had a higher stiffness and smaller loss factor compared to that prepared from 304, with 4.46% higher energy consumption and significantly better overall performance than the 304 material.

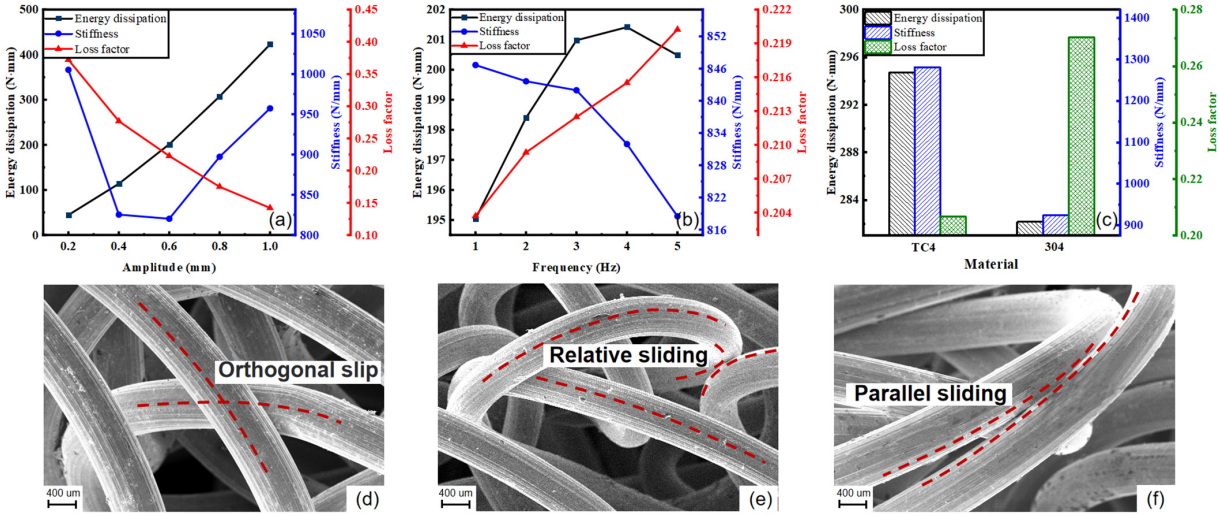

Figure 8. Results of dynamic experiments: (**a**–**c**) Effects of amplitude, frequency and material on the dynamic performance of lumbar fusion apparatus (**d**–**f**) metal-rubber core wire contact state.

4.3. Impact Resistance Performance of Lumbar Fusion Cage

To further investigate the biomechanical performance of lumbar fusion cages under different excitation amplitudes, pulse widths, and materials, impact tests with various operating conditions were conducted on an impact test bench. The parameters of the test groups are listed in Table 4, with Groups A, B, and C being the amplitude test group, pulse width test group, and material test group, respectively.

Table 4. Impact test parameters for each group.

Test Group Number	Impact Amplitude (g)	Impact Pulse Width (ms)	Relative Density (g/cm^3)	Relative Density (mm)	Material
A1	5	21	1.5	0.2	TC4
A2	7	21	1.5	0.2	TC4
A3	9	21	1.5	0.2	TC4
B1	9	21	1.5	0.2	TC4
B2	9	16	1.5	0.2	TC4
B3	9	11	1.5	0.2	TC4
C1	9	21	1.5	0.2	TC4
C2	9	21	1.5	0.2	304

To further study the impact resistance of the lumbar fusion cage, the impact isolation coefficient and kinetic energy decay rate were introduced as evaluation indices of the impact biomechanical properties.

(1) Impact isolation coefficient

The impact isolation factor is an important indicator for evaluating the impact resistance of the lumbar fusion cage. The ratio of the maximum magnitude of the response acceleration to that of the excitation acceleration is often expressed, and the impact isolation coefficient η can be calculated as follows:

$$\eta = \frac{a\prime_{\max}}{a_{\max}} \tag{8}$$

where $a_{\max}$ is the maximum amplitude of the excitation acceleration, and $a\prime_{\max}$ is the maximum amplitude of the response acceleration.

(2) Kinetic energy decay rate

The kinetic energy decay rate, i.e., the ratio of the kinetic energy decayed by the system in the first decay cycle to the initial kinetic energy, was employed to quantify the energy decay of the LFD during impact; the kinetic energy decay rate ψ can be defined as follows:

$$\psi = \frac{E_1 - E_2}{E_1} = 1 - \frac{E_2}{E_1} \tag{9}$$

where E_1 is the kinetic energy of the system when the response velocity reaches its first peak after the impact load has been applied, and E_2 is the kinetic energy of the system when the response velocity reaches its second peak.

4.4. Analysis of Impact Test Results

The experimental acceleration excitation curves for different impact amplitudes, pulse widths, and materials are shown in Figure 9a–c, and the corresponding acceleration response curves for the lumbar fusion cage are presented in Figure 9d–f. It can be observed that, upon impact, the MR located inside the lumbar fusion deformed rapidly. The increase in the contact points between the internal wires resulted in a rapid increase in the non-linear stiffness, which, through the friction and slippage between the internal wires, dissipated the impact energy and rapidly reduced the kinetic energy within the system, allowing it to quickly return to a stable state. It can also be deduced that the lower the shock amplitude and the smaller the pulse width to which the fusion is subjected, the sooner the system will return to stability, while a change in the material will have little effect on that time.

Figure 10 exhibits the variation of the impact resistance parameters of the fusion device with different impact amplitudes, pulse widths, and materials. In particular, Figure 10a–c show the variation of the peak acceleration response and the time to the peak response with amplitude, pulse width, and material, respectively. It can be found that: (1) as the impact amplitude increased, the peak acceleration response gradually increased and the response arrival time gradually decreased; (2) As the pulse width increased, the peak acceleration response gradually increased, with the response reaching a slight decrease in the peak time from 11 ms to 16 ms, and then increasing, exhibiting an overall increasing trend; (3) The peak acceleration response of the lumbar fusion prepared by TC4 was higher than that of the lumbar fusion prepared by 304 and its response arrival time was lower than that of the lumbar fusion prepared by 304. Figure 10d–f demonstrate the impact isolation factor and kinetic energy decay rate as a function of the shock amplitude, pulse width, and material, respectively. In Figure 10d, it can be seen that both the impact isolation coefficient and kinetic energy decay rate tended to decrease with increasing impact amplitude, indicating that the impact resistance of the fusion device increased with increasing impact amplitude. This is due to the fact that the deformation of the MR inside the LFD increases with increasing impact amplitude, which increases the number of contact points between the

wire turns inside the fusion device, and can also lead to wire orthogonal contact sliding (Figure 8d) and relative contact sliding (Figure 8e) in some intertwined wire areas. While under load, the angle of the wire distribution changes, causing a shift to parallel contact sliding (Figure 8f), thereby allowing the energy of the impact to be dissipated. According to Figure 10e, the impact isolation factor changed very little with increasing impact amplitude under a pulse width ranging from 11 ms to 16 ms, and then exhibited an overall tendency to increase; the kinetic energy decay rate increased slightly between 11 ms and 16 ms, and then decreased. In Figure 10f, it can be observed that the impact isolation factor and the kinetic energy decay rate of the lumbar fusion prepared by TC4 were higher compared to that prepared by 304, with a 3.14% increase in the kinetic energy decay rate, providing excellent impact resistance.

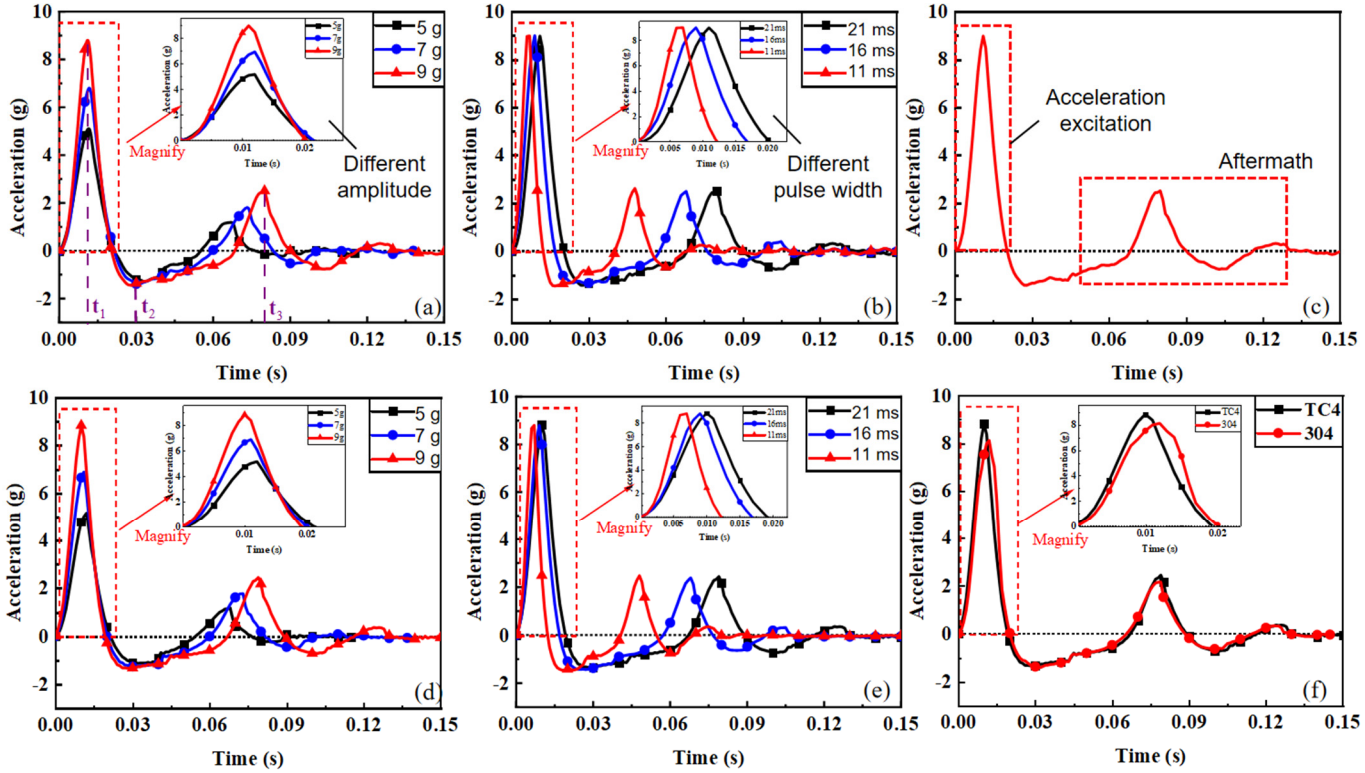

Figure 9. Acceleration excitation and response curves under different impact conditions: (**a**–**c**) acceleration excitation curves for different impact amplitudes, pulse widths, and materials, respectively; (**d**–**f**) acceleration response curves for different impact amplitudes, pulse widths, and materials, respectively.

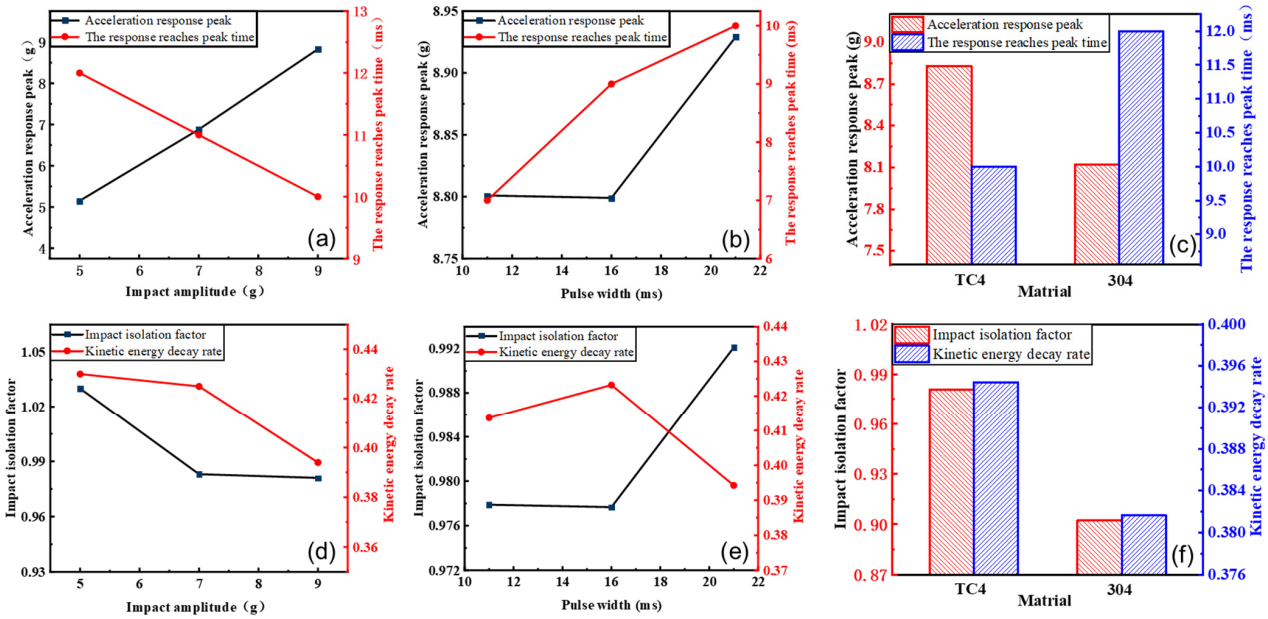

Figure 10. Impact resistance variation charts: (**a**,**d**) diagram of impact resistance variation with impact amplitude; (**b**,**e**) chart of impact resistance with pulse width; (**c**,**f**) image of impact resistance changing with material.

5. Conclusions

A lateral approach symmetric lumbar fusion cage was designed by introducing an LTA-FMP MR material with damping characteristics. A lumbar spine model was reconstructed and structural design of the symmetric lumbar fusion model was performed via reverse engineering based on CT data of the lumbar intervertebral disc. Through FE simulations, dynamic and quasi-static mechanical and impact resistance tests, evaluation indices such as the loss factor, impact isolation factor, and kinetic energy decay rate were introduced to comprehensively evaluate its comprehensive biomechanical performance. The main research elements and conclusions are as follows:

(1) The lumbar vertebral spacing parameters at the L3/L4 segment were determined by modified CT measurements to guide the structural design of the lumbar spinal fusion cage. The fusion cage was designed using a CoCrMo frame and TC4 medical titanium alloy MR. The L3/L4 segment lumbar spine model was reconstructed using reverse engineering and assembled with an LFD to obtain the stress distribution on the upper and lower bone endplates and perform von Mises stress analysis under various conditions. Comparative analysis of results reported in the relevant literature was also conducted. The designed lumbar fusion cage had a significantly lower peak stress under all loading conditions, which significantly reduces the sink probability of the fusion cage, while the peak von Mises stress was significantly lower than the 203 MPa value reported in the relevant literature, indicating a lower risk of collapse after implantation.

(2) An innovative LTA-FMP MR core with a spatial microporous structure was introduced, and the lumbar fusion core parameters were designed by means of forward design. Quasi-static tests with different force gradients were performed and it was found that as the relative density was increased, the energy dissipation and loss factor of the LTA-FMP MR core tended to decrease, while the static stiffness tended to increase. The core of the LFD prepared from TC4 with a filament diameter of 0.2 mm and a relative density of 1.5 g/cm^3 achieved an energy dissipation of 32.62 N·mm and exhibited good energy dissipation characteristics.

(3) A biomechanical test platform was built to analyze the mechanical properties under sinusoidal excitation with different amplitudes and frequencies, as well as impact

loads with different amplitudes and pulse widths. In-depth and comprehensive assessment of the biomechanical performance of the lumbar fusion cage was performed by introducing the loss factor, impact isolation factor, and kinetic energy decay rate evaluation indices. It was demonstrated that, as the amplitude was increased, the energy dissipation of the symmetric lumbar fusion gradually increased and the loss factor gradually decreased; however, its stiffness tended to decrease first and then increase. As the vibration frequency increased, the stiffness gradually decreased and the loss factor gradually increased, while the energy dissipation exhibited a trend of increasing first and then decreasing. The impact isolation factor and kinetic energy decay rate of the lumbar fusion decreased with increasing impact amplitude. As the pulse width was increased, the impact isolation factor tended to overall increase and the kinetic energy decay rate tended to increase first and then decrease. Compared to that prepared from 304, the lumbar fusion cage prepared from TC4 had a lower loss factor, a higher impact isolation factor, a 4.46% increase in energy dissipation, and a 3.14% increase in kinetic energy decay rate, possessing superior biomechanical properties.

Author Contributions: Software, J.X. (Juan Xiao); Formal analysis, T.Z.; Investigation, T.Z.; Resources, J.X. (Jian Xu); Data curation, L.L.; Writing—original draft, J.X. (Juan Xiao); Visualization, Z.R.; Supervision, L.S.; Project administration, J.X. (Jian Xu); Funding acquisition, Z.R. All authors have read and agreed to the published version of the manuscript.

Funding: We thank the National Safety Academic Fund of China-NSAF (Grant No. U2330202); The National Natural Science Foundation of China (Grant No. 52175162, 51805086 and 51975123); Key Technologies Innovation and Industrialization Projects in Fujian Province (Grant No. 2023XQ005).

Data Availability Statement: The data used to support the findings of this study are available from the corresponding author upon request.

Conflicts of Interest: The authors declare no conflict of interest.

References

1. Umale, S.; Yoganandan, N.; Baisden, J.L.; Choi, H.; Kurpad, S.N. A biomechanical investigation of lumbar interbody fusion techniques. *J. Mech. Behav. Biomed. Mater.* **2022**, *125*, 104961. [CrossRef] [PubMed]
2. Shi, L.; Liu, M.; Liu, Y.; Zhao, Q.; Cheng, K.; Zhang, H.; Fathollahi-Fard, A.M. Evaluation of Urban Traffic Accidents Based on Pedestrian Landing Injury Risks. *Appl. Sci.* **2022**, *12*, 6040. [CrossRef]
3. Lee, H.J.; Lee, S.J.; Jung, J.; Lee, T.H.; Jeong, C.; Lee, T.J.; Jang, J.E.; Lee, J.W. Biomechanical Evaluation of Lateral Lumbar Interbody Fusion with Various Fixation Options for Adjacent Segment Degeneration: A Finite Element Analysis. *World Neurosurg.* **2023**, *173*, e156–e167. [CrossRef] [PubMed]
4. Hou, Q.; Zhu, Q.; Wu, Y.; Li, R.; Li, D.; Zhang, Y.; Ruan, Q. Animal modelling of lumbar corpectomy and fusion and in vivo growth of spine supporting bone by titanium cage implants: An experimental study. *J. Bionic Eng.* **2010**, *7*, 329–336. [CrossRef]
5. Oikawa, R.; Murakami, H.; Endo, H.; Yan, H.; Yamabe, D.; Chiba, Y.; Oikawa, R.; Nishida, N.; Chen, X.; Sakai, T.; et al. Comparison of the susceptibility to implant failure in the lateral, posterior, and transforaminal lumbar interbody fusion: A finite element analysis. *World Neurosurg.* **2022**, *164*, e835–e843. [CrossRef]
6. Luoma, J.; Saarenpää, I.; Rinne, J.; Frantzén, J.; Moritz, N.; Vallittu, P.K. Quasi-static loading of glass fiber-reinforced composite cervical fusion cage. *J. Mech. Behav. Biomed. Mater.* **2022**, *136*, 105481. [CrossRef]
7. Zhang, Z.; Liao, Z.; Sun, Y.; Sun, X.; Liu, W. Biomechanical Research Progress of Lumbar Interbody Cage and Lumbar Interbody Fusion. *J. Med. Biomech.* **2018**, *6*, E465–E470.
8. Guzman, J.Z.; Iatridis, J.C.; Skovrlj, B.; Cutler, H.S.; Hecht, A.C.; Qureshi, S.A.; Cho, S.K. Outcomes and complications of diabetes mellitus on patients undergoing degenerative lumbar spine surgery. *Spine* **2014**, *39*, 1596. [CrossRef]
9. Carpenter, R.D.; Klosterhoff, B.S.; Torstrick, F.B.; Foley, K.T.; Burkus, J.K.; Lee, C.S.; Gall, K.; Guldberg, R.E.; Safranski, D.L. Effect of porous orthopaedic implant material and structure on load sharing with simulated bone ingrowth: A finite element analysis comparing titanium and PEEK. *J. Mech. Behav. Biomed. Mater.* **2018**, *80*, 68–76. [CrossRef]
10. Palmquist, A.; Snis, A.; Emanuelsson, L.; Browne, M.; Thomsen, P. Long-term biocompatibility and osseointegration of electron beam melted, free-form–fabricated solid and porous titanium alloy: Experimental studies in sheep. *J. Biomater. Appl.* **2013**, *27*, 1003–1016. [CrossRef]
11. Luo, Y.; Jiang, H.; Cheng, G.; Liu, H. Effect of carburization on the mechanical properties of biomedical grade titanium alloys. *J. Bionic Eng.* **2011**, *8*, 86–89. [CrossRef]

12. Pattanayak, D.K.; Fukuda, A.; Matsushita, T.; Takemoto, M.; Fujibayashi, S.; Sasaki, K.; Nishida, N.; Nakamura, T.; Kokubo, T. Bioactive Ti metal analogous to human cancellous bone: Fabrication by selective laser melting and chemical treatments. *Acta Biomater.* **2011**, *7*, 1398–1406. [CrossRef] [PubMed]
13. Chen, Z.; Tong, J.; Li, X.; Yan, Y. The advantages and disadvantages of interbody implantation materials in the treatment of lumbar fusion. *China Tissue Eng. Res.* **2022**, *26*, 1597–1603.
14. Moussa, A.; Tanzer, M.; Pasini, D. Cervical fusion cage computationally optimized with porous architected Titanium for minimized subsidence. *J. Mech. Behav. Biomed. Mater.* **2018**, *85*, 134–151. [CrossRef] [PubMed]
15. Harrysson, O.L.A.; Cansizoglu, O.; Marcellin-Little, D.J.; Cormier, D.R.; West, H.A., II. Direct metal fabrication of titanium implants with tailored materials and mechanical properties using electron beam melting technology. *Mater. Sci. Eng. C* **2008**, *28*, 366–373. [CrossRef]
16. Heinl, P.; Müller, L.; Körner, C.; Singer, R.F.; Müller, F.A. Cellular Ti–6Al–4V structures with interconnected macro porosity for bone implants fabricated by selective electron beam melting. *Acta Biomater.* **2008**, *4*, 1536–1544. [CrossRef]
17. Liu, J.; Tang, J.; Liu, H. Comparison of One versus Two Cages in Lumbar Interbody Fusion for Degenerative Lumbar Spinal Disease: A Meta-analysis. *Orthop. Surg.* **2014**, *6*, 236–243. [CrossRef]
18. Herrera, A.; Yánez, A.; Martel, O.; Afonso, H.; Monopoli, D. Computational study and experimental validation of porous structures fabricated by electron beam melting: A challenge to avoid stress shielding. *Mater. Sci. Eng. C* **2014**, *45*, 89–93. [CrossRef]
19. Butscher, A.; Bohner, M.; Hofmann, S.; Gauckler, L.; Müller, R. Structural and material approaches to bone tissue engineering in powder-based three-dimensional printing. *Acta Biomater.* **2011**, *7*, 907–920. [CrossRef]
20. Wang, Z.; Feng, H.; Ma, X.; Chen, C.; Deng, C.; Sun, L. Effectiveness of three-dimensional printing artificial vertebral body and interbody fusion cage in anterior cervical surgery. *Chin. J. Reparative Reconstr. Surg.* **2021**, *35*, 1147–1154.
21. Luo, L.; Yu, S.; Yu, Z.; Liu, C.; Han, J.; Niu, J. Advantages and clinical application status of 3D printing titanium and titanium alloy medical devices. *Biomeopathic Mater. Clin. Res.* **2015**, *12*, 72–75. (In Chinese)
22. Levine, B.R.; Sporer, S.; Poggie, R.A.; Della Valle, C.J.; Jacobs, J.J. Experimental and clinical performance of porous tantalum in orthopedic surgery. *Biomaterials* **2006**, *27*, 4671–4681. [CrossRef] [PubMed]
23. Yang, H.; Li, J.; Zhou, Z.; Ruan, J. Structural preparation and biocompatibility evaluation of highly porous Tantalum scaffolds. *Mater. Lett.* **2013**, *100*, 152–155. [CrossRef]
24. Zardiackas, L.D.; Parsell, D.E.; Dillon, L.D.; Mitchell, D.W.; Nunnery, L.A.; Poggie, R. Structure, metallurgy, and mechanical properties of a porous tantalum foam. *J. Biomed. Mater. Res.* **2001**, *58*, 180–187. [CrossRef] [PubMed]
25. Levine, B. A new era in porous metals: Applications in orthopaedics. *Adv. Eng. Mater.* **2008**, *10*, 788–792. [CrossRef]
26. Patel, M.S.; McCormick, J.R.; Ghasem, A.; Huntley, S.R.; Gjolaj, J.P. Tantalum: The next biomaterial in spine surgery? *J. Spine Surg.* **2020**, *6*, 72. [CrossRef] [PubMed]
27. Shen, L.; Ren, Z.; Xu, J.; Pan, L.; Lin, Y.; Bai, H. Dry friction damping mechanism of flexible microporous metal rubber based on cell group energy dissipation mechanism. *Friction* **2023**, *11*, 259–279. [CrossRef]
28. Fu, J. Experimental Evaluation of Friction and Wear Properties of Artificial Hip Joint Materials. Ph.D. Dissertation, Harbin Institute of Technology, Harbin, China, 2009.
29. He, G.; Liu, P.; Tan, Q.; Jiang, G. Flexural and compressive mechanical behaviors of the porous titanium materials with entangled wire structure at different sintering conditions for load-bearing biomedical applications. *J. Mech. Behav. Biomed. Mater.* **2013**, *28*, 309–319. [CrossRef]
30. Zhao, X. Simulation Analysis and Experimental Study on Motion of Metal Rubber Artificial Intervertebral Disc. Master's Thesis, Harbin Institute of Technology, Harbin, China, 2021.
31. Bach, K.; Ford, J.; Foley, R.; Januszewski, J.; Murtagh, R.; Decker, S.; Uribe, J.S. Morphometric analysis of lumbar intervertebral disc height: An imaging study. *World Neurosurg.* **2019**, *124*, e106–e118. [CrossRef]
32. Qin, S.; Li, J.; Xu, Y.; Guo, F.; Jiang, Y.; Shen, S.; Xu, Y. Application of modified CT measurement in the evaluation of lumbar intervertebral height. *Curr. Med.* **2021**, *27*, 4–6. (In Chinese)
33. Gu, X.; Jia, L.; Chen, X.; Lu, C.; Liu, Y.; Zhang, D. Establishment and verification of three-dimensional finite element model of lumbar spondylolysis. *Med. Biomech.* **2010**, *25*, 45–50. (In Chinese)
34. Zhang, W.; Wang, L.; Shi, Q.; Zeng, S.; Yang, H.; Luo, Z. Finite element analysis of lumbar vertebra fixation by foraminal approach. *Med. Biomech.* **2014**, *29*, 405–410. (In Chinese)
35. Knutsen, A.R.; Borkowski, S.L.; Ebramzadeh, E.; Flanagan, C.L.; Hollister, S.J.; Sangiorgio, S.N. Static and dynamic fatigue behavior of topology designed and conventional 3D printed bioresorbable PCL cervical interbody fusion devices. *J. Mech. Behav. Biomed. Mater.* **2015**, *49*, 332–342. [CrossRef] [PubMed]
36. Wang, H.; Wan, Y.; Li, Q.; Xia, Y.; Liu, X.; Liu, Z.; Li, X. Porous fusion cage design via integrated global-local topology optimization and biomechanical analysis of performance. *J. Mech. Behav. Biomed. Mater.* **2020**, *112*, 103982. [CrossRef]